

# PROCEEDINGS OF SPIE

[SPIDigitalLibrary.org/conference-proceedings-of-spie](https://spiedigitallibrary.org/conference-proceedings-of-spie)

## PixDD: a multi-pixel silicon drift detector for high-throughput spectral-timing studies

F. Ceraudo, F. Ambrosino, P. Bellutti, G. Bertuccio, G. Borghi, et al.

F. Ceraudo, F. Ambrosino, P. Bellutti, G. Bertuccio, G. Borghi, R. Campana, M. Caselle, D. Cirrincione, I. Dedolli, E. Del Monte, Y. Evangelista, M. Feroci, F. Ficorella, M. Fiorini, F. Fuschino, M. Gandola, M. Grassi, C. Labanti, P. Loffredo, G. Lombardi, P. Malcovati, F. Mele, A. Morbidini, R. Piazzolla, A. Picciotto, A. Rachevski, I. Rashevskaya, A. Tobia, A. Vacchi, A. Volpe, G. Zampa, N. Zampa, N. Zorzi, "PixDD: a multi-pixel silicon drift detector for high-throughput spectral-timing studies," Proc. SPIE 12191, X-Ray, Optical, and Infrared Detectors for Astronomy X, 1219116 (29 August 2022); doi: 10.1117/12.2630450

**SPIE.**

Event: SPIE Astronomical Telescopes + Instrumentation, 2022, Montréal, Québec, Canada

# PixDD: a multi-pixel Silicon Drift Detector for high-throughput spectral-timing studies

F. Ceraudo<sup>a</sup>, F. Ambrosino<sup>b</sup>, P. Bellutti<sup>c</sup>, G. Bertuccio<sup>d</sup>, G. Borghi<sup>c</sup>, R. Campana<sup>e,f</sup>, M. Caselle<sup>g</sup>, D. Cirrincione<sup>h,i</sup>, I. Dedolli<sup>d</sup>, E. Del Monte<sup>a,j</sup>, Y. Evangelista<sup>a,j</sup>, M. Feroci<sup>a,j</sup>, F. Ficorella<sup>c</sup>, M. Fiorini<sup>k</sup>, F. Fuschino<sup>e</sup>, M. Gandola<sup>c,d</sup>, M. Grassi<sup>l</sup>, C. Labanti<sup>e</sup>, P. Loffredo<sup>a</sup>, G. Lombardi<sup>a</sup>, P. Malcovati<sup>l</sup>, F. Mele<sup>d</sup>, A. Morbidini<sup>a</sup>, R. Piazzolla<sup>m</sup>, A. Picciotto<sup>c</sup>, A. Rachevski<sup>h</sup>, I. Rashevskaya<sup>h,n</sup>, A. Tobia<sup>a</sup>, A. Vacchi<sup>i</sup>, A. Volpe<sup>m</sup>, G. Zampa<sup>h</sup>, N. Zampa<sup>h,i</sup>, and N. Zorzi<sup>c</sup>

<sup>a</sup>INAF/IAPS-Roma, Via del Fosso del Cavaliere, 100, I-00133, Rome, Italy

<sup>b</sup>INAF/OAR-Roma, Via Frascati, 33, I-00040, Monte Porzio Catone, Italy

<sup>c</sup>Fondazione Bruno Kessler, Via Sommarive, 18, I-38123, Povo, Italy

<sup>d</sup>Politecnico di Milano, Via Anzani, 42, I-22100, Como, Italy

<sup>e</sup>INAF/OAS-Bologna, Via Piero Gobetti, 93, I-40129, Bologna, Italy

<sup>f</sup>INFN, Sezione di Bologna, Viale C. Berti Pichat, 6/2, I-40127, Bologna, Italy

<sup>g</sup>Karlsruher Institut für Technologie, Hermann-von-Helmholtz-Platz, 1, D-76344, Eggenstein-Leopoldshafen, Germany

<sup>h</sup>INFN, Sezione di Trieste, Località Padriciano, 99, I-34149, Trieste, Italy

<sup>i</sup>University of Udine, Via delle Scienze, 206, I-33100, Udine, Italy

<sup>j</sup>INFN, Sezione di Roma Tor Vergata, Viale della Ricerca Scientifica, 1, I-00133, Roma, Italy

<sup>k</sup>INAF/IASF-Milano, Via Alfonso Corti, 12, I-20133, Milano, Italy

<sup>l</sup>University of Pavia, Via Ferrata, 5, I-27100 Pavia, Italy

<sup>m</sup>Italian Space Agency, Via del Politecnico, I-00133, Rome, Italy

<sup>n</sup>TIFPA, Via Sommarive, 14, I-38123, Povo, Italy

## ABSTRACT

The *Pixelated silicon Drift Detector* (PixDD) is a two-dimensional multi-pixel X-ray sensor based on the technology of Silicon Drift Detectors, designed to solve the dead time and pile-up issues of photon-integrating imaging detectors. Read out by a two-dimensional self-triggering Application-Specific Integrated Circuit named RIGEL, to which the sensor is bump-bonded, it operates in the 0.5 – 15 keV energy range and is designed to achieve single-photon sensitivity and good spectroscopic capabilities even at room temperature or with mild cooling (< 150 eV resolution at 6 keV at 0 °C). The paper reports on the design and performance tests of the 128-pixel prototype of the fully integrated system.

**Keywords:** X-ray spectroscopy, Time-resolved spectroscopy, Silicon Drift Detectors, X-ray timing, Single-photon detectors

## 1. INTRODUCTION

High energy radiation from astrophysical objects is among the most useful messengers to study the behaviour of matter under the extreme conditions of gravity, density and magnetism, that cannot be replicated on Earth. In particular, the spectral distribution and time variability of the sources is a useful tool that can help constrain the theoretical models and shed light upon the physics involved in some of the most violent phenomena in the universe.

---

(Send correspondence to F. Ceraudo)

F. Ceraudo: E-mail: francesco.ceraudo@inaf.it

X-Ray, Optical, and Infrared Detectors for Astronomy X, edited by Andrew D. Holland, James Beletic  
Proc. of SPIE Vol. 12191, 1219116 · © 2022 SPIE · 0277-786X · doi: 10.1117/12.2630450

Thanks to the maturity of the technology of both optics and radiation sensors, the 0.5 – 10 keV band is particularly suitable for this investigation. When imaging is not the primary concern, lighter and more compact optical systems can be adopted, e.g. *lobster-eye* optics, for which the Point Spread Function (PSF) can be in the order of one millimetre.<sup>1,2</sup> The optimal pixel of a sensor underneath the optical system should therefore have small enough pixels to oversample the PSF, but at the same time large enough pixels to limit charge sharing and number of readout channels.

Detectors such as Si-PIN sensors have the important drawback of a large anode capacitance ( $\sim$  pF), requiring long shaping times which are incompatible with high-throughput astronomy. Moreover, their spectral performances are not suitable for Fano-limited applications, especially when cooling power is not abundant. Likewise, despite being the most widespread technology in the field, Charged-Coupled Devices (CCDs) suffer from limitations, mainly due to them being charge-integrating devices, thus requiring low operating temperatures<sup>3-5</sup> ( $< -70^\circ\text{C}$ ) to limit the build-up of leakage current in the pixels. Furthermore, they are affected by dead time and pile-up, particularly relevant in case of high-rate sources, and are therefore not suitable for photon-by-photon spectral-timing studies under those circumstances. Newer technologies such as Depleted p-channel Field Effect Transistors<sup>6-8</sup> (DEPFETs) have excellent spectral and imaging capabilities, whose readout frame rates can reach 10 kHz in the case of space astronomy missions,<sup>9</sup> or even a few MHz on ground.<sup>10</sup> However, such operation still requires a high power consumption, which poses some issues for satellite applications.

The PixDD project, short for *Pixelated silicon Drift Detector*, aims to develop an alternative multi-pixel system based on the technology of Silicon Drift Detectors.<sup>11,12</sup> The device is to operate in the 0.5 – 15 keV band and it is to achieve good spectral resolution already at room temperature or with mild cooling (FWHM  $\lesssim$  150 eV at 6 keV at  $0^\circ\text{C}$ ). This goal becomes possible thanks to the development of a custom Application Specific Integrated Circuit (ASIC), named RIGEL,<sup>13</sup> to which the sensor is coupled via a bump-bonding process. The project is a collaboration between the Italian National Institute for Astrophysics (INAF), with overall PI-ship and responsibility for device testing, the National Institute for Nuclear Physics (INFN), in charge of the design of the sensor, Bruno Kessler Foundation (FBK), responsible for the production of the detector, Polytechnic of Milan and University of Pavia, for the design of the ASIC, and the Karlsruhe Institute of Technology (KIT), in charge of the ASIC-to-sensor bump-bonding integration.

In this paper, the first characterization of an integrated PixDD-RIGEL system is presented. After an overview of the sensor (Sec. 2) and the integration process with its readout chip (Sec. 3), the overall spectral features are evaluated (Sec. 4), followed by an assessment of the sub-pixel response (Sec. 5).

## 2. THE PIXDD SENSOR

The PixDD sensor design takes advantage of the lateral depletion mechanism used in Silicon Drift Detectors to reduce the size of the collecting anode, which translates into a smaller detector capacitance. This is a paramount requirement to be able to perform soft X-ray spectroscopy with Fano-limited energy resolution.

Realized on a 450  $\mu\text{m}$ -thick  $n$ -type  $\langle 100 \rangle$ -silicon substrate with a resistivity of about 9 k $\Omega$  cm, the detector is subdivided into 128 pixels arranged in a  $16 \times 8$  matrix (Fig. 1). Each pixel has a square aspect ratio with a 300  $\mu\text{m}$ -side, chosen to match the typical Point Spread Function of lobster-eye optics. The anode is a circular  $n^+$  implant with a diameter of 40  $\mu\text{m}$  covered by an aluminium pad of the same size. A 28  $\mu\text{m}$ -circular opening of the SiO<sub>2</sub> passivation layer of the sensor is arranged to allow the connection with the front-end ASIC by means of gold-stud bumping and bonding (Sec. 3). Two  $p^+$  cathodes surround the anodes, the inner one (called Low Voltage cathode, C<sub>LV</sub>) has a circular shape on the anode side, with a non-implanted gap of 10  $\mu\text{m}$ , and a square shape (with rounded corners) on the side facing the second cathode (High Voltage cathode, C<sub>HV</sub>) which is shared between neighbouring pixels. The gap between C<sub>HV</sub> and C<sub>LV</sub> is 60  $\mu\text{m}$ -wide in order to maximize the punch-through threshold voltage  $V_{\text{thr,PT}}$  between the two cathodes, defined as the voltage where the punch-through current equals the leakage current of the cathodes. Due to the high resistivity of the substrate,  $V_{\text{thr,PT}} \approx 8$  V at the operative bias. An  $n$ -spray implant controls the equivalent oxide charge in the gap between the cathodes, natively very low in the FBK production process. This very delicate region is furthermore shielded from environmental influences thanks to a positive field plate connected to C<sub>LV</sub>.

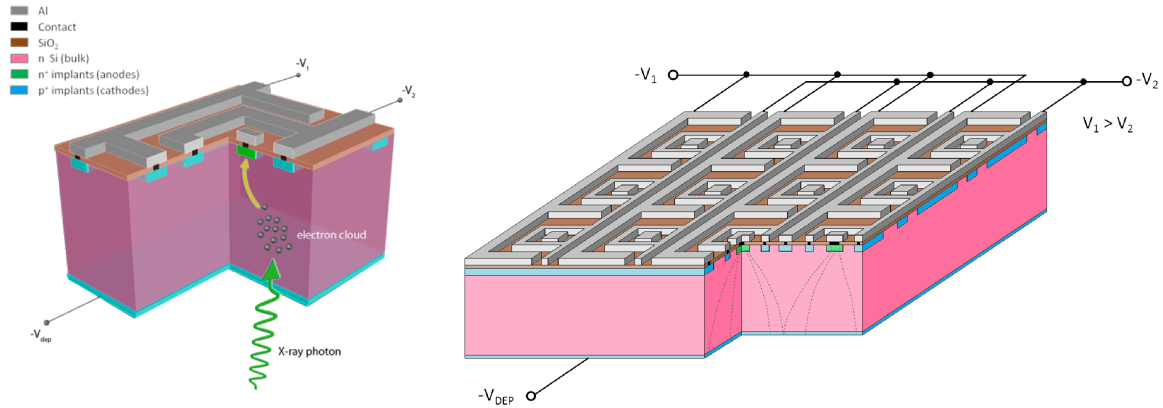


Figure 1: Simplified view of the PixDD sensor. *Left*: single pixel. *Right*: matrix.

On the opposite face of the detector, a shallow  $p^+$  implant covering the full pixel array area is used as an entrance window for the X-ray photons with a sizeable sensitivity down to the  $C - K_{\alpha}$  energy<sup>14</sup> (277 eV). To allow the peripheral pixels to maintain the same sensitive area of the inner ones, the entrance window extends  $450\ \mu\text{m}$  toward the edge of the device, and a  $p^+$  implant, biased at the same potential as  $C_{LV}$ , faces this region.

The full depletion of the sensor is reached with the window implant at  $-70\ \text{V}$ , while  $C_{LV}$  and  $C_{HV}$  are biased at  $-32\ \text{V}$  and  $-39\ \text{V}$  respectively. The FBK production process uses dedicated steps to reduce the leakage current to below few hundreds  $\text{pA cm}^{-2}$  at room temperature (even reaching  $< 50\ \text{pA cm}^{-2}$ , as in Ref. 15), thus each pixel of PixDD can potentially have a sub-pA leakage current at room temperature. Together with an anode capacitance  $\leq 35\ \text{fF}$ , such a low dark current allows to obtain Fano-limited energy resolutions without sensor cooling, although this result also depends on the front-end ASIC and the coupling between the two devices.

### 3. THE BONDING PROCESS

The PixDD sensor is coupled with a RIGEL ASIC, which reads out the anodes and also provides the biases of both  $C_{LV}$  and  $C_{HV}$ . The connection between the two devices is enabled by a bump-bonding technique, which ensures both an excellent fill factor of the sensitive area (i.e. fraction of successful bondings), and low parasitic capacitance (i.e. good noise performances). To reduce the production costs typical of traditional bump-bonding processes, and mainly due to photolithography, a novel bump-bonding technology has been developed at KIT.<sup>16</sup> Based on gold-stud bonding, this technique is able to produce metal bumps with diameters down to  $30\ \mu\text{m}$ , and can also be tailored to specific detectors.

As a first step of the integration between the RIGEL and the detector, gold studs are placed on the specifically designed passivation openings present on both the front-end cells of the ASIC and the anodes of the sensor (*bumping phase*). This procedure requires bumps no larger than  $40\ \mu\text{m}$  and a position accuracy of only a few micrometers (Fig. 2a).

After that, the proper bonding is performed via thermo-mechanical compression, i.e. the two devices are heated up and they are pressed together, allowing their respective gold studs to connect (*flip-chip bonding*). In this case, the pick-and-place accuracy is better than  $1\ \mu\text{m}$  between sensor and readout circuit. This feature, combined with the optimised value of the bond force, temperature and process duration, results in high mechanical strength and excellent electrical performance. Fig. 2b shows a cross-section of the final structure. After the flip-chip process, the distance between the sensor and the ASIC is about  $23\ \mu\text{m}$  with a final deformation of the bumps measuring less than  $50\ \mu\text{m}$ .

### 4. SPECTRAL RESPONSE

To assess the spectral performances of the system, the detector was illuminated with a radioactive  $^{55}\text{Fe}$  source. All measurements were taken in a thermally controlled room at a temperature of  $20\ ^{\circ}\text{C}$ . At this stage of the

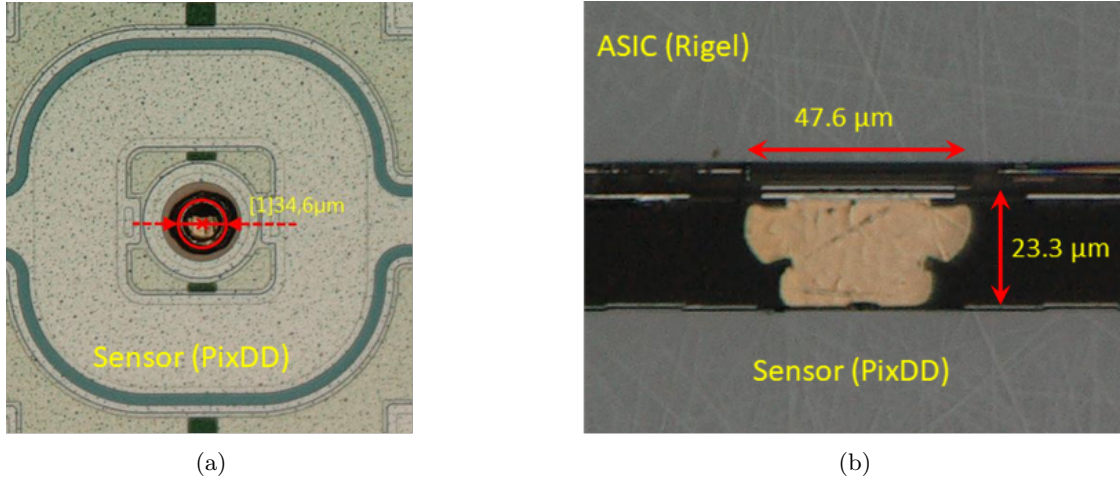


Figure 2: Details of the bump-bonding process. Fig. 2a: gold-stud bump on the PixDD sensor cell. Fig. 2b: cross-section of the bump-bonding between sensor and readout chip.

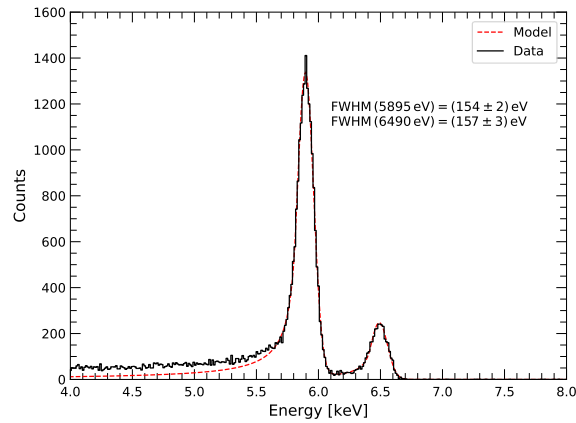


Figure 3:  $^{55}\text{Fe}$  spectrum recorded at  $T = 20\text{ }^\circ\text{C}$  for a sample pixel.

characterisation, only one ASIC channel was activated at a time. The reason for this pixel-by-pixel acquisition procedure came from the limited data transfer rate of the UART link between the FPGA and the control PC, which stably supported only a rate of a few events per second, thus making matrix-wide acquisitions impractical for detailed laboratory characterisation, due to the long exposure time they would otherwise require.

It must be noted that, from the start, a few pixels presented a very high low-energy noise level that could not be reduced by adjusting the discriminator threshold. The corresponding ASIC channels were therefore switched off for the entirety of the tests, implying that no characterisation with radioactive source was possible for them.

Fig. 3 shows the  $^{55}\text{Fe}$  spectrum measured by a sample pixel. Both the  $\text{Mn} - \text{K}_\alpha$  and the  $\text{Mn} - \text{K}_\beta$  lines (at 5895 eV and 6490 eV respectively) feature noticeable low-energy tails, due to the incomplete photon charge collection inside the pixel under study, which in turn results from charge sharing between neighbouring pixels (this aspect will be discussed in further detail in Sec. 5). For this reason, instead of the customary Gaussian profiles, it was decided to fit the spectral lines by using a Crystal Ball function,<sup>17</sup> defined as

$$G(E; E_0, \sigma, \alpha, n, G_0) = \frac{G_0}{\sigma(C + D)} \begin{cases} \exp\left[-\frac{(E-E_0)^2}{2\sigma^2}\right] & \text{if } \frac{E-E_0}{\sigma} > -\alpha \\ \frac{A}{B - \left(\frac{E-E_0}{\sigma}\right)^n} & \text{if } \frac{E-E_0}{\sigma} \leq -\alpha \end{cases} \quad (1)$$

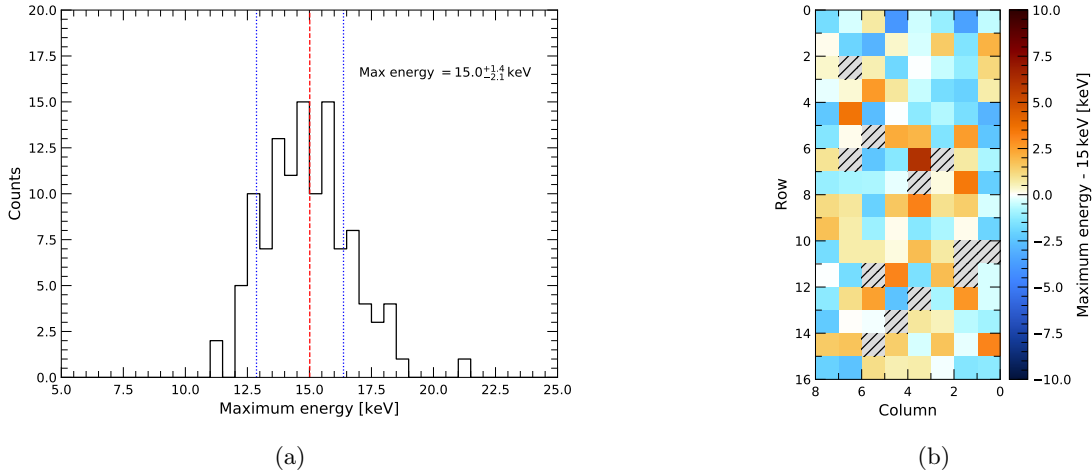


Figure 4: Maximum measurable energy of all active pixels at  $T = 20\text{ }^{\circ}\text{C}$ . Fig. 4a: histogram of the recorded values. Fig. 4b: map of the pixel-wise deviation from the goal value of 15 keV. In the map, hatched pixels were deactivated during acquisitions because of their high low-energy noise.

where

$$\begin{aligned}
 A &= \left( \frac{n}{|\alpha|} \right)^n \exp\left(-\frac{\alpha^2}{2}\right) \\
 B &= \frac{n}{|\alpha|} - |\alpha| \\
 C &= \frac{n}{|\alpha|} \exp\left(-\frac{\alpha^2}{2}\right) / (n-1) \\
 D &= \sqrt{\frac{\pi}{2}} \left[ 1 + \operatorname{erf}\left(\frac{|\alpha|}{\sqrt{2}}\right) \right].
 \end{aligned}$$

In the previous formulas,  $G_0$  is a normalisation factor,  $E_0$  is the line center, and  $\sigma$  is the standard deviation of the associated Gaussian profile, whereas  $\alpha$  and  $n$  define its low-energy exponential tail. The Crystal Ball curve takes into account the effects of partial charge collection, thus it limits the uncertainty deriving from choosing the fitting intervals. The conversion from ADC units to electronvolts is then performed via a linear fit on the calculated spectral line centres. The energy resolution is finally estimated as the Gaussian Full-Width at Half Maximum (FWHM) of the line profiles, i.e.  $\text{FWHM} = 2\sqrt{2\log 2}\sigma$ , with  $\sigma$  resulting from the Crystal Ball fit. The fitting and calibration procedure is repeated on all active pixels of the matrix.

Fig. 4a presents the histogram of the maximum photon energy that can be recorded by each pixel, calculated as the largest possible ADC reading (i.e. 1023 ADU) converted to energy, given the specific pixel-wise gain-offset calibration. The most probable value of the distribution is exactly the design goal of 15 keV, with a dispersion, calculated as the boundaries of the Highest Density Region (HDR), of 10 – 15% (68%-HDR), compatible with the inter-channel variability due to the fabrication process of the ASIC. If the geometrical distribution of the pixels on the matrix is taken into account, as in Fig. 4b, no trend is apparent, and the distribution is flat within the fluctuations.

The histogram of the energy resolution (FWHM) at the Mn –  $K_{\alpha}$  line measured for each pixel is reported in Fig. 5a for a shaping time of  $\tau = 1.8\text{ }\mu\text{s}$ . The distribution is peaked around  $158_{-7}^{+141}\text{ eV}$  and is clearly asymmetrical, presenting a long tail towards larger line widths. Once the position of these hot pixels on the detector matrix is taken into account (Fig. 5b), a large cluster of particularly poor-performing pixels becomes evident in the lower half of the detector, with two elongated structures penetrating into the upper half. This is likely to be the result of several defects on the entrance window of the sensor, formed during the flip-chip phase of the bonding process. This conclusion is drawn from the fact that the pixels in question have performances comparable to every other

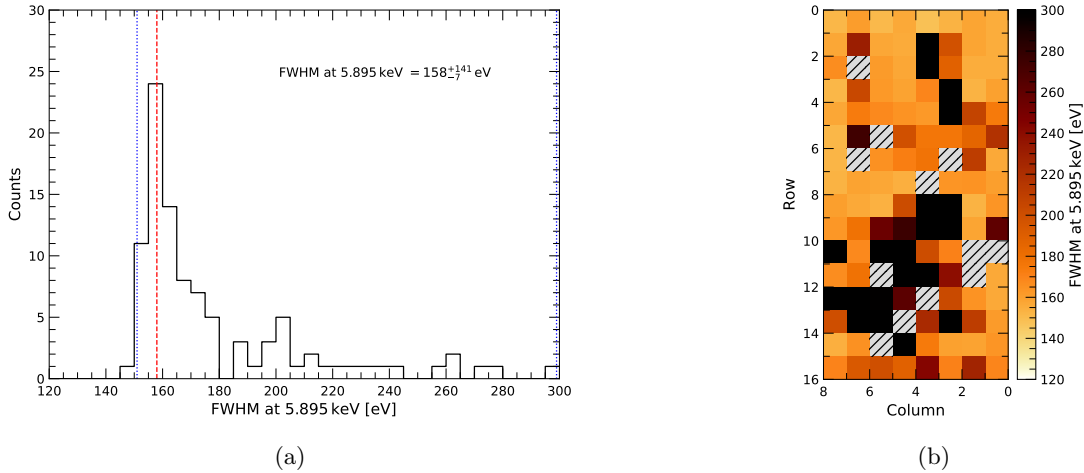


Figure 5: Energy resolution (FWHM of the Mn –  $K_{\alpha}$  line) of all active pixels at  $T = 20^{\circ}\text{C}$  and  $\tau = 1.8\ \mu\text{s}$ . Fig. 5a: histogram of the recorded values. Fig. 5b: map of the recorded values. In the map, hatched pixels were deactivated during acquisitions because of their high low-energy noise.

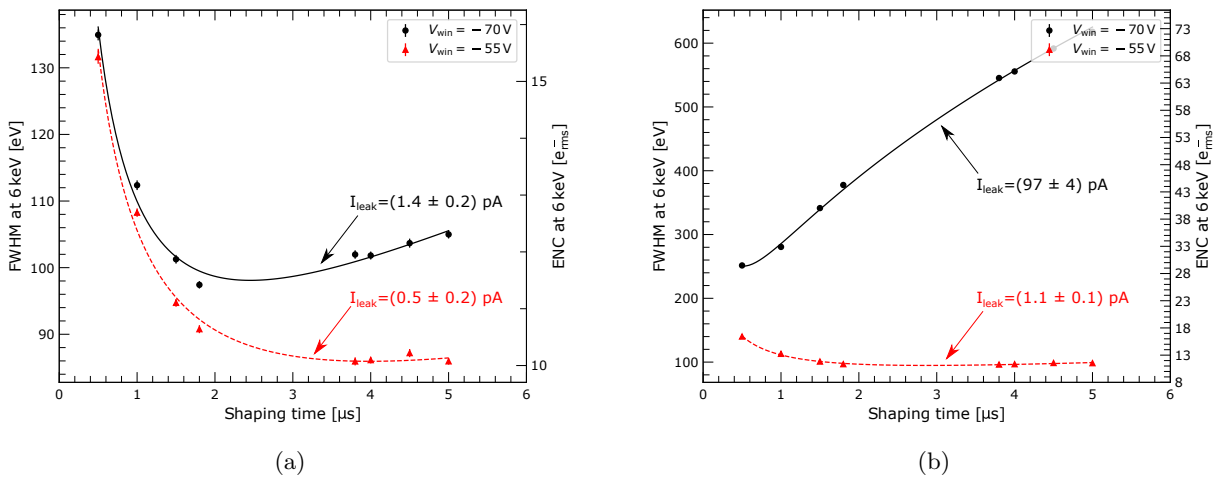


Figure 6: Energy resolution as a function of shaping time and voltage applied to the entrance window. At  $V_{\text{win}} = -55\ \text{V}$ , the anodes are not connected to the bulk yet, therefore the leakage current of the detector is negligible. At  $V_{\text{win}} = -70\ \text{V}$ , i.e. the nominal mode of operation, the dark current of the sensor reaches the anodes. Measurements were done by injecting an artificial charge of  $\approx 1653\ e^{-}$  (corresponding to 6 keV in silicon) to the test capacitors connected to the input pad of each analogue RPC of the RIGEL ASIC. Fig. 6a: pixel with coordinates (4,2) in Fig. 5b. Fig. 6b: pixel with coordinates (2,4) in Fig. 5b.

pixel when the bias on the window is so low that the anodes are not connected to the bulk of the detector, implying that both the anodes and the front-end channels of the RIGEL ASIC are working properly. On the other hand, the curves of the spectral resolution versus shaping time (Fig. 6) highlight that largest contribution to the noise of the hot pixels at nominal bias is the leakage current, which can be as high as two orders of magnitude with respect to the value measured on the sensor before its integration with the ASIC (measured at an average of a few pA per anode). The most probable explanation is therefore that the mechanical stresses involved in the flip-chip bonding damaged the thin photon entrance window, thus causing the onset of several charge generation centres.

If the calibrated events recorded by all active channels are considered together, the  $^{55}\text{Fe}$  spectrum of Fig. 7a is obtained. For the whole system at room temperature, the energy resolution at the Mn –  $K_{\alpha}$  line is then  $(191.2 \pm 0.3)\ \text{eV}$ , corresponding to an Equivalent Noise Charge (ENC) of  $(17.69 \pm 0.05)\ e_{\text{rms}}^{-}$ . If the noisiest

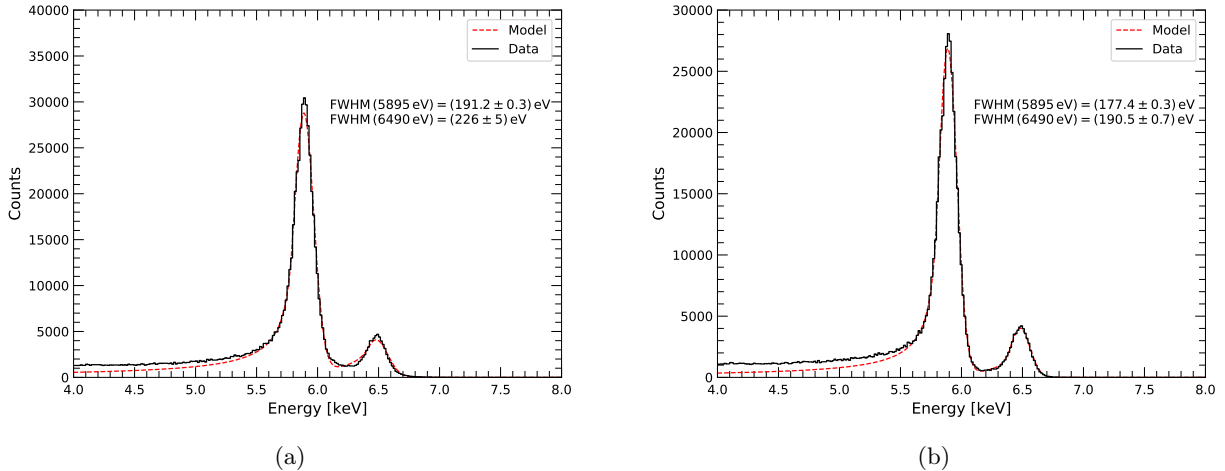


Figure 7: Spectrum obtained by considering the calibrated events of the pixel-wise acquisitions at  $T = 20^\circ\text{C}$  and  $\tau = 1.8\ \mu\text{s}$ . Fig. 7a: sum spectrum of all active pixels. Fig. 7b: sum spectrum of all active pixels featuring a spectral resolution better than 300 eV.

(most damaged) pixels are left out of the calculation by considering only those featuring a resolution better than 300 eV at 5.9 keV, the results is the spectrum in Fig. 7b, whose resolution then becomes  $(177.4 \pm 0.3)\ \text{eV}$ , corresponding to  $\text{ENC} = (15.61 \pm 0.05)\ e_{\text{rms}}^-$ .

## 5. SUB-PIXEL RESPONSE

The sub-pixel response was investigated in the X-ray facility of the INAF-IAPS laboratories in Rome.<sup>18</sup> Photons from a commercial Fe-anode X-ray tube were collimated through a custom system to obtain a beam with a  $\text{FWHM} \approx 20\ \mu\text{m}$  at the surface of the detector. Motorized linear stages allowed to position the beam with micrometric precision.

A  $400\ \mu\text{m} \times 400\ \mu\text{m}$  square region roughly centred around the pixel located at coordinates (4, 6) was selected for the study, and 121 positions, placed on a  $40\ \mu\text{m}$ -pitch grid, were illuminated. It is worth noting that the region was purposely chosen larger than a single  $300\ \mu\text{m} \times 300\ \mu\text{m}$ -pixel in order to investigate the pixel boundaries. Hence, a total of nine pixels were illuminated during the scan. However, two of them, i.e. (3, 6) and (5, 5), had to be switched off due to unfavourable environmental conditions that made them temporarily noisy. For the same reason, the threshold of the discriminators had to be kept at  $\approx 1.5\ \text{keV}$ .

Photon events were selected according to their multiplicity, i.e. the number of ASIC channels triggering at the same time, to study the onset of charge sharing between neighbouring pixels. Fig. 8 shows the spatial distribution of single events across the tested region of the detector, while Fig. 9 present the same for double events. For each pixel, a flat central region is visible, spanning  $\approx 280\ \mu\text{m} \times 280\ \mu\text{m}$ , where all counts are recorded essentially by that pixel alone. Charge sharing occurs in a  $\approx 40\ \mu\text{m}$ -wide boundary region between two neighbouring pixels, although this is influenced by the low-energy threshold of each involved pixel. Even though they are not presented for the sake of clarity due to their low statistics, the maps illustrating triple and quadruple events also behave according to expectations, i.e. all multiple events are concentrated around the corners of the pixels.

## 6. CONCLUSIONS

In this paper, the first characterisation of the PixDD-RIGEL integrated system was presented. The spectral measurements taken at room temperature were demonstrated to be consistent with the design goal of  $\text{FWHM} \lesssim 150\ \text{eV}$  at 6 keV at  $0^\circ\text{C}$ . Although this was true for a large portion of the sensor pixels, a significant number of them showed sub-optimal performances, due to a strong localised leakage current. This phenomenon was interpreted as the result of defects on the thin entrance window, generated during the flip-chip phase of the bump-bonding between the detector and the readout chip.

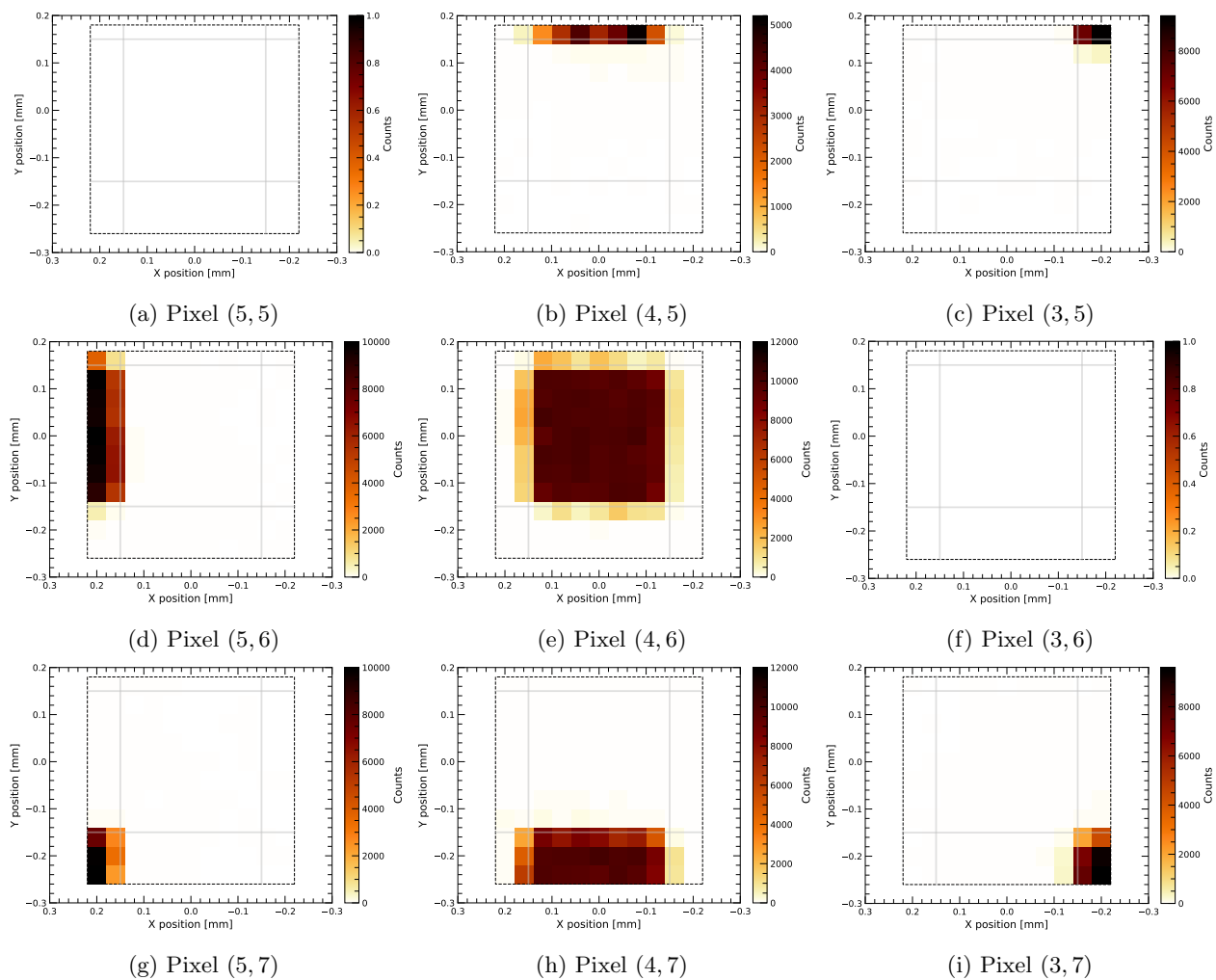


Figure 8: Spatial distribution of single events around pixel (4,6). In each plot,  $x$  and  $y$  indicate the physical distance with respect to the centre of pixel (4,6). The investigated region is enclosed with the dashed line, whereas the solid grey lines indicate the pixel boundaries. Pixels (5,5) and (3,6) were switched off during the tests.

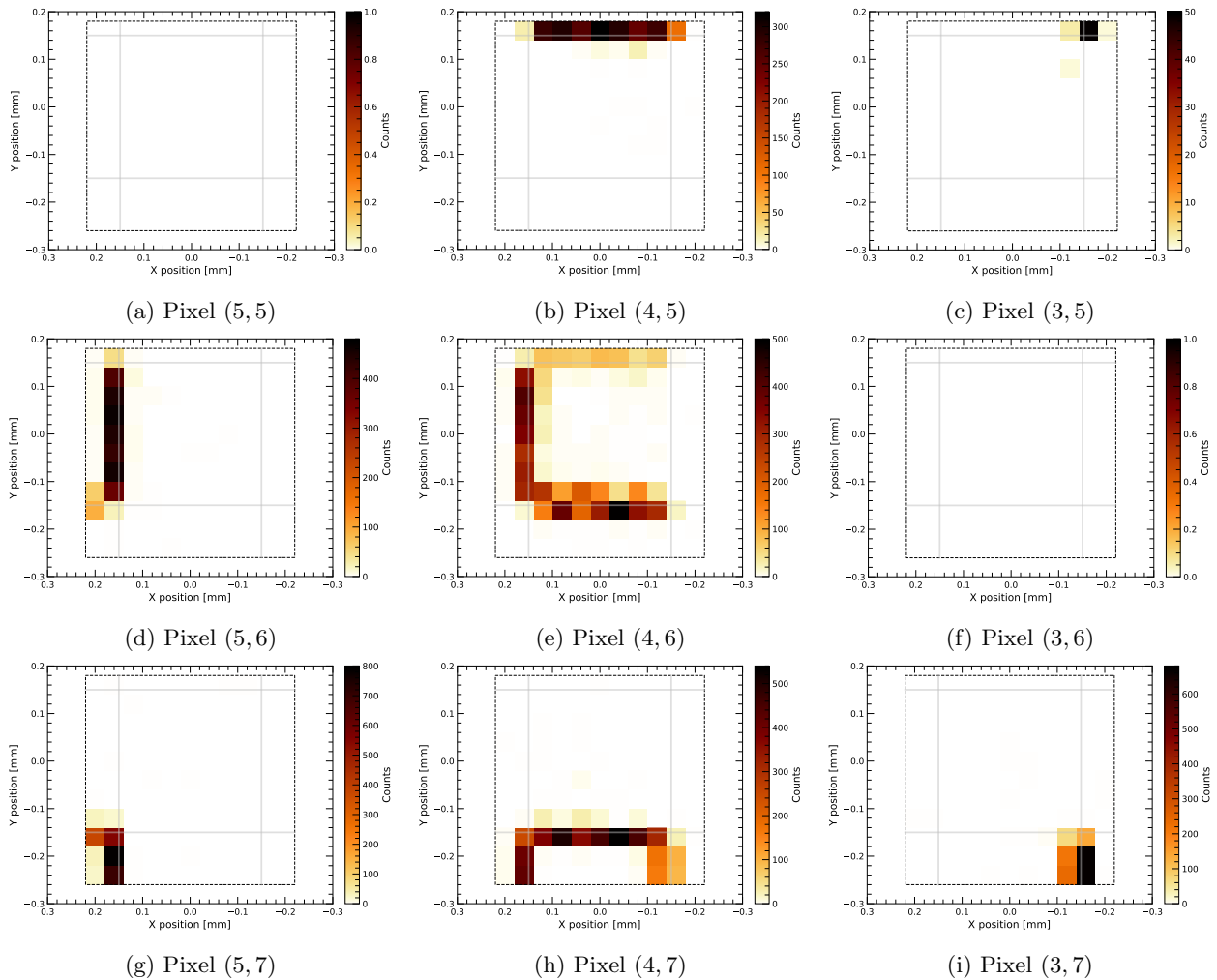


Figure 9: Spatial distribution of double events around pixel (4,6). In each plot,  $x$  and  $y$  indicate the physical distance with respect to the centre of pixel (4,6). The investigated region is enclosed with the dashed line, whereas the solid grey lines indicate the pixel boundaries. Pixels (5,5) and (3,6) were switched off during the tests.

The sub-pixel and inter-pixel response of the sensor was studied thanks to a micrometric X-ray beam, which allowed to investigate the regions inside a cell and between neighbouring pixels. No zones with sub-optimal charge collection were encountered, and charge sharing was measured to occur only in a limited band across the boundaries between pixels.

Investigations are ongoing to solve the damaging of the sensor during bump-bonding, and more samples of the integrated system are expected to be available for characterisation in a short time. Other aspects of the response are also yet to be tested, such as the behaviour at lower temperatures, as well as the timing performances.

## ACKNOWLEDGMENTS

This work was carried out within the scope of the *Advanced Detector for X-ray Astronomy* (ADAM) programme, founded by the Italian Space Agency (research agreement 2018-11-HH.0).

## REFERENCES

- [1] Feldman, C., Pearson, J., Willingale, R., Sykes, J., Drumm, P., Houghton, P., Bicknell, C., Osborne, J., Martindale, A., O'Brien, P., Fairbend, R., Schyns, E., Petit, S., Roudot, R., Mercier, K., Le Duigou, J.-M., and Gotz, D., "Testing and modelling of the SVOM MXT narrow field lobster-eye telescope," in [*Society of Photo-Optical Instrumentation Engineers (SPIE) Conference Series*], *Society of Photo-Optical Instrumentation Engineers (SPIE) Conference Series* **10399**, 103991Q (Aug. 2017).
- [2] Yuan, W., Zhang, C., Ling, Z., Zhao, D., Wang, W., Chen, Y., Lu, F., Zhang, S.-N., and Cui, W., "Einstein Probe: a lobster-eye telescope for monitoring the x-ray sky," in [*Space Telescopes and Instrumentation 2018: Ultraviolet to Gamma Ray*], den Herder, J.-W. A., Nikzad, S., and Nakazawa, K., eds., *Society of Photo-Optical Instrumentation Engineers (SPIE) Conference Series* **10699**, 1069925 (July 2018).
- [3] Strüder, L., Briel, U., Dennerl, K., Hartmann, R., Kendziorra, E., Meidinger, N., Pfeiffermann, E., Reppin, C., Aschenbach, B., Bornemann, W., Bräuninger, H., Burkert, W., Elender, M., Freyberg, M., Haberl, F., Hartner, G., Heuschmann, F., Hippmann, H., Kastelic, E., Kemmer, S., Kettenring, G., Kink, W., Krause, N., Müller, S., Oppitz, A., Pietsch, W., Popp, M., Predehl, P., Read, A., Stephan, K. H., Stötter, D., Trümper, J., Holl, P., Kemmer, J., Soltau, H., Stötter, R., Weber, U., Weichert, U., von Zanthier, C., Carathanassis, D., Lutz, G., Richter, R. H., Solc, P., Böttcher, H., Kuster, M., Staubert, R., Abbey, A., Holland, A., Turner, M., Balasini, M., Bignami, G. F., La Palombara, N., Villa, G., Buttler, W., Gianini, F., Lainé, R., Lumb, D., and Dhez, P., "The European Photon Imaging Camera on XMM-Newton: The pn-CCD camera," *Astronomy and Astrophysics* **365**, L18–L26 (Jan. 2001).
- [4] Turner, M. J. L., Abbey, A., Arnaud, M., Balasini, M., Barbera, M., Belsole, E., Bennie, P. J., Bernard, J. P., Bignami, G. F., Boer, M., Briel, U., Butler, I., Cara, C., Chabaud, C., Cole, R., Collura, A., Conte, M., Cros, A., Denby, M., Dhez, P., Di Coco, G., Dowson, J., Ferrando, P., Ghizzardi, S., Gianotti, F., Goodall, C. V., Gretton, L., Griffiths, R. G., Hainaut, O., Hochedez, J. F., Holland, A. D., Jourdain, E., Kendziorra, E., Lagostina, A., Laine, R., La Palombara, N., Lortholary, M., Lumb, D., Marty, P., Molendi, S., Pigot, C., Poindron, E., Pounds, K. A., Reeves, J. N., Reppin, C., Rothenflug, R., Salvatet, P., Sauvageot, J. L., Schmitt, D., Sembay, S., Short, A. D. T., Spragg, J., Stephen, J., Strüder, L., Tiengo, A., Trifoglio, M., Trümper, J., Vercellone, S., Vigroux, L., Villa, G., Ward, M. J., Whitehead, S., and Zonca, E., "The European Photon Imaging Camera on XMM-Newton: The MOS cameras," *Astronomy and Astrophysics* **365**, L27–L35 (Jan. 2001).
- [5] Meidinger, N., Andritschke, R., Bornemann, W., Coutinho, D., Emberger, V., Hälker, O., Kink, W., Mican, B., Müller, S., Pietschner, D., Predehl, P., and Reiffers, J., "Report on the eROSITA camera system," in [*Space Telescopes and Instrumentation 2014: Ultraviolet to Gamma Ray*], Takahashi, T., den Herder, J.-W. A., and Bautz, M., eds., *Society of Photo-Optical Instrumentation Engineers (SPIE) Conference Series* **9144**, 91441W (July 2014).
- [6] Kemmer, J. and Lutz, G., "New detector concepts," *Nuclear Instruments and Methods in Physics Research A* **253**, 365–377 (Jan. 1987).
- [7] Kemmer, J., Lutz, G., Prechtel, U., Schuster, K., Sterzik, M., Strüder, L., and Ziemann, T., "Experimental confirmation of a new semiconductor detector principle," *Nuclear Instruments and Methods in Physics Research A* **288**, 92–98 (Mar. 1990).

- [8] Lutz, G., Richter, R. H., and Strüder, L., “Novel pixel detectors for X-ray astronomy and other applications,” *Nuclear Instruments and Methods in Physics Research A* **461**, 393–404 (Apr. 2001).
- [9] Meidinger, N., Barbera, M., Emberger, V., Fürmetz, M., Manhart, M., Müller-Seidlitz, J., Nandra, K., Plattner, M., Rau, A., and Treberspurg, W., “The Wide Field Imager instrument for Athena,” in [*Society of Photo-Optical Instrumentation Engineers (SPIE) Conference Series*], *Society of Photo-Optical Instrumentation Engineers (SPIE) Conference Series* **10397**, 103970V (Aug. 2017).
- [10] Porro, M., Andricek, L., Aschauer, S., Bayer, M., Becker, J., Bombelli, L., Castoldi, A., De Vita, G., Diehl, I., Erdinger, F., Facchinetti, S., Fiorini, C., Fischer, P., Gerlach, T., Graafsma, H., Guazzoni, C., Hansen, K., Kalavakuru, P., Klar, H., Kugel, A., Lechner, P., Lemke, M., Lutz, G., Manghisoni, M., Mezza, D., Muntefering, D., Pietsch, U., Quartieri, E., Randall, M., Re, V., Reckleben, C., Sandow, C., Soldat, J., Struder, L., Szymanski, J., Weidenspointner, G., and Wunderer, C. B., “Development of the DEPFET Sensor With Signal Compression: A Large Format X-Ray Imager With Mega-Frame Readout Capability for the European XFEL,” *IEEE Transactions on Nuclear Science* **59**, 3339–3351 (Dec. 2012).
- [11] Gatti, E. and Rehak, P., “Semiconductor drift chamber — An application of a novel charge transport scheme,” *Nuclear Instruments and Methods in Physics Research* **225**, 608–614 (Sept. 1984).
- [12] Evangelista, Y., Ambrosino, F., Feroci, M., Bellutti, P., Bertuccio, G., Borghi, G., Campana, R., Caselle, M., Cirrincione, D., Ficorella, F., Fiorini, M., Fuschino, F., Gandola, M., Grassi, M., Labanti, C., Malcovati, P., Mele, F., Morbidini, A., Picciotto, A., Rachevski, A., Rashevskaya, I., Sammartini, M., Zampa, G., Zampa, N., Zorzi, N., and Vacchi, A., “Characterization of a novel pixelated Silicon Drift Detector (PixDD) for high-throughput X-ray astrophysics,” *Journal of Instrumentation* **13**, P09011 (Sept. 2018).
- [13] Gandola, M., Grassi, M., Mele, F., Dedolli, I., Malcovati, P., and Bertuccio, G., “The Sparse Readout RIGEL Application Specific Integrated Circuit for Pixel Silicon Drift Detectors in Soft X-Ray Imaging Space Applications.”
- [14] Bufon, J., Altissimo, M., Aquilanti, G., Bellutti, P., Bertuccio, G., Billè, F., Borghes, R., Borghi, G., Cautero, G., Ciano, S., Cicuttin, A., Cirrincione, D., Crespo, M. L., Fabiani, S., Ficorella, F., Gandola, M., Gianoncelli, A., Giuressi, D., Grisonich, R., Kourousias, G., Mannatunga, K. S., Mele, F., Menk, R. H., Olivi, L., Orzan, G., Picciotto, A., Rachevski, A., Rashevskaya, I., Sammartini, M., Schillani, S., Stofa, A., Zampa, G., Zampa, N., Zorzi, N., and Vacchi, A., “Large solid angle and high detection efficiency multi-element silicon drift detectors (SDD) for synchrotron based x-ray spectroscopy,” in [*Synchrotron Radiation Instrumentation - SRI2018*], *American Institute of Physics Conference Series* **2054**, 060061 (Jan. 2019).
- [15] Bertuccio, G., Ahangarianabhari, M., Graziani, C., Macera, D., Shi, Y., Gandola, M., Rachevski, A., Rashevskaya, I., Vacchi, A., Zampa, G., Zampa, N., Bellutti, P., Giacomini, G., Picciotto, A., Piemonte, C., and Zorzi, N., “X-Ray Silicon Drift Detector-CMOS Front-End System with High Energy Resolution at Room Temperature,” *IEEE Transactions on Nuclear Science* **63**, 400–406 (Feb. 2016).
- [16] Caselle, M., Blank, T., Colombo, F., Dierlamm, A., Husemann, U., Kudella, S., and Weber, M., “Low-cost bump-bonding processes for high energy physics pixel detectors,” *Journal of Instrumentation* **11**, C01050 (Jan. 2016).
- [17] Skwarnicki, T., *A study of the radiative CASCADE transitions between the Upsilon-Prime and Upsilon resonances*, PhD thesis, Cracow, INP (1986).
- [18] Muleri, F., Soffitta, P., Bellazzini, R., Brez, A., Costa, E., Frutti, M., Mastropietro, M., Morelli, E., Pinchera, M., Rubini, A., and Spandre, G., “A versatile facility for the calibration of x-ray polarimeters with polarized and unpolarized controlled beams,” in [*Space Telescopes and Instrumentation 2008: Ultraviolet to Gamma Ray*], Turner, M. J. L. and Flanagan, K. A., eds., *Society of Photo-Optical Instrumentation Engineers (SPIE) Conference Series* **7011**, 701127 (July 2008).